OPEN ACCESS



Multispecies Energetic Particle Acceleration Associated with CIR and ICME-driven Shocks

Ashok Silwal¹, Lingling Zhao^{1,2}, Gary P. Zank^{1,2}, Bingbing Wang², Alexander Pitña³, Sujan Prasad Gautam¹,

Byeongseon Park³, Masaru Nakanotani², and Xingyu Zhu²,

¹ Department of Space Science, The University of Alabama in Huntsville, AL, USA; Iz0009@uah.edu

² Center for Space Plasma and Aeronomic Research (CSPAR), The University of Alabama in Huntsville, Huntsville, AL, USA

³ Charles University, Faculty of Mathematics and Physics, Prague, Czech Republic

**Received 2024 January 3; revised 2024 July 6; accepted 2024 July 8; published 2024 September 5

Abstract

A multispecies energetic particle intensity enhancement event at 1 au is analyzed. We identify this event as a corotating interaction region (CIR) structure that includes a stream interface (SI), a forward-reverse shock pair, and an embedded heliospheric current sheet (HCS). The distinct feature of this CIR event is that (1) the high-energy (>1 MeV) ions show significant flux enhancement at the reverse wave (RW)/shock of the CIR structure, following their passage through the SI and HCS. The flux amplification appears to depend on the energy per nucleon. (2) Electrons in the energy range of 40.5–520 keV are accelerated immediately after passing through the SI and HCS regions, and the flux quickly reaches a peak for low-energy electrons. At the RW, only high-energy electrons (~520 keV) show significant local flux enhancement. The CIR structure is followed by a fast-forward perpendicular shock driven by a coronal mass ejection (CME), and we observed a significant flux enhancement of low-energy protons and high-energy electrons. Specifically, the 210-330 keV proton and 180-520 keV electron fluxes are enhanced by approximately 2 orders of magnitude. This suggests that the later ICME-driven shock may accelerate particles out of the suprathermal pool. In this paper, we further present that for CIR-accelerated particles, the increase in turbulence power at SI and RWs may be an important factor for the observed flux enhancement in different species. The presence of ion-scale waves near the RW, as indicated by the spectral bump near the proton gyrofrequency, suggests that the resonant wave-particle interaction may act as an efficient energy transferrer between energetic protons and ion-scale waves.

Unified Astronomy Thesaurus concepts: Solar energetic particles (1491); Solar wind (1534); Corotating streams (314)

1. Introduction

Large-scale transient disturbances from the Sun, especially solar flares and coronal mass ejections (CMEs), can cause sudden changes in the properties of the solar wind and particles can be accelerated to GeV per nucleon (Cane & Lario 2006). In addition to solar flares and CMEs, which occur more frequently during high solar activity epochs, stream interaction regions (SIRs) are also important sources of energetic particles, particularly during the declining phase of the solar cycle (Richardson et al. 1993; Jian et al. 2006). A SIR is formed by the interaction between the trailing fast solar wind and the preceding slower solar wind. If a SIR is quasi-steady with a recurrent structure, then this kind of compression region is often referred as corotating interaction regions (CIRs; Belcher & Davis 1971; Jian et al. 2008). CIRs can form a pair of shocks; one propagating forward into the slow solar wind, the "forward" shock, and another propagating sunward into the fast solar wind, the "reverse" shock (Jian et al. 2006; Li 2017; Richardson 2018). CIRs can substantially accelerate energetic particles to several MeV per nucleon at the reverse and/or forward shocks (Giacalone & Jokipii 1997; Richardson 2004, 2018; Zhao et al. 2019) via the diffusive shock acceleration (DSA; Krymskii 1977; Bell 1978; Blandford &

Original content from this work may be used under the terms of the Creative Commons Attribution 4.0 licence. Any further distribution of this work must maintain attribution to the author(s) and the title of the work, journal citation and DOI.

Ostriker 1978; Drury 1983) mechanism. Previous studies have shown that reverse shock is more often associated with energetic particle enhancements than forward shock. However, recent observations (Allen et al. 2021; Wei et al. 2022) have shown that the energetic particle enhancement is not always confined to the CIR-associated reverse shock. Instead, the enhancement starts at the stream interface (SI) and extends well into the fast stream. In particular, Allen et al. (2020) found that the suprathermal particle enhancement at 1 au starts at the SI and stretches into the fast-stream solar wind for over a day. The confinement of the suprathermal particles to the SI suggests that these particles are locally accelerated, and are probably related to non-shock-related acceleration processes. A similar argument was presented by Wei et al. (2022). They investigated the intensity enhancement of energetic ions associated with an SIR during the decay phase of a gradual solar energetic particle event using STEREO-A data. They found that the intensities of low-energy ions (<300 keV nuc⁻¹) peak at the forward-reverse shock pair, while the intensities of high-energy ions peak at the SI. By combining the detailed study of the energy spectra in different regions, they concluded that the low-energy ions are accelerated by the shocks, and the high-energy ions are accelerated by non-shock-associated mechanisms. Furthermore, compression regions without shocks can also induce a first-order Fermi acceleration process (Webb et al. 1983; Giacalone et al. 2002; Sokolov et al. 2006). This occurs when the spatial extent of the compression is significantly smaller than the particle mean free path, such that the particles experience the compression wave as if it were

a shock (Giacalone et al. 2002). In addition, a second-order Fermi acceleration may also contribute to the local ion acceleration in SIRs (e.g., Richardson 1985; Schwadron et al. 1996, 2021). As such, comprehensive studies of SIRs and their associated suprathermal and energetic components observed within 1 au provide insight into both the formation of SIRs and any associated acceleration occurring near and within the CIRs.

The energy spectra of energetic particles associated with CIRs are different from those associated with typical flares or CMEs (Mason et al. 1997; Desai et al. 1999; Richardson 2004). For typical CIR events, the spectra of all particle species observed at 1 au tend to have an exponential shape (Gloeckler et al. 1979; Mewaldt et al. 1979). In comparison, a CMErelated solar energetic particle (SEP) event often has a powerlaw energy spectrum. The energy spectra of energetic particles associated with SIR events at 1 au have been well modeled by Fisk & Lee (1980). In this model, particles are accelerated through multiple shock crossings at the forward or reverse shock located at $3 \sim 5$ au and transported back to 1 au along the field lines, yielding a modulation effect at low energies due to convection and adiabatic cooling in the expanding solar wind. At sufficiently large distances from the source region, the spectrum rolls over at low energies as those particles are unable to penetrate far enough into the inner heliosphere to reach the observer. The predicted energy spectral shape shows qualitative agreement with observations. However, some early observations (Mason et al. 1997; Ebert et al. 2012) found that the particle energy spectra observed during CIR events generally do not exhibit significant modulation effects (turnover) at low energies. Recent Parker Solar Probe (PSP) observations of the inner heliosphere (McComas et al. 2019) also do not show lowenergy turnovers, suggesting that sub-Parker field lines may allow more direct access to the shock region. To further better understand some of the observed features of SEP events, the geometry of the shock and magnetic field and its variation over time has to be taken into consideration. These features have been shown to have a substantial effect on the local acceleration and measured particle intensities (e.g., McComas & Schwadron 2006; Guo et al. 2010).

Although the basic mechanisms related to energetic particle release and acceleration are fairly well known in principle, electrically charged particles are subjected to multiple complicated physical processes between their origin and an observer in interplanetary (IP) space. One aspect of particle acceleration that has not been investigated in great detail in the solar wind is the acceleration of particles at multiple shocks. As discussed above and further below, shocks are frequently found as pairs in CIR events or even triplets and it is unclear how the gross morphology and global structure of these events affect the energization of charged particles and their distribution functions. In this work, we investigate a CIR event observed by the WIND spacecraft on 2011 February 14–15, during the inclining phase of solar cycle 24. An SI mixed with a heliospheric current sheet (HCS) and a forward-reverse shock/wave pair is observed along with several prominent features: (a) the CIR event is followed by an ICME so that the entire event consists of three consecutive IP shocks and (b) the CIR particles demonstrate deviation from theoretical predictions of classical shock-related acceleration processes. The flux enhancement at the three shocks and the SI is different for each species, suggesting that different mechanisms may be responsible for the acceleration of ions and electrons. This paper is organized

as follows. In Section 2, we review the WIND observations during 2011 February 14 00:00 UT–February 19 00:00 UT and examine protons, electrons, and helium flux enhancement during the period. Section 3 shows the evolution of the energetic particle spectra. In Section 4, we investigate the evolution of the magnetic fluctuation level and establish the possible connection between fluctuation strength and CIR particle acceleration. Section 5 discusses the pitch angle distributions (PADs) of the energetic particles. The last section provides a summary and conclusions.

2. Overview of WIND Observation

The event under study was caused by three Earth-directed CMEs launched during 2011 February 13–15 from NOAA AR 11158 (Mishra & Srivastava 2014). These CMEs interacted with each other en route and were revealed as a complex magnetic structure at 1 au in WIND data. We identified a CIR structure from the in situ observation, as shown in Figure 1. The leading edge of the CIR is bounded by a fast shock (hereinafter FS1), whereas the trailing edge shows a reverse wave (RW) that has not yet steepened into a shock.

From Figure 1, we see that the magnetic field strength |B|, the proton number density n_p and the electron number density n_e , the proton temperature T_p and the electron temperature T_e , the total pressure P, and the solar wind speed V all show a sudden increase or decrease at the boundaries of the shaded region. The changes at the leading edge are slightly more significant than those at the trailing edge, implying a CIR structure with the forward shock observed at 15:06 UT on February 14 and the RW at 19:00 UT on February 15. The SI associated with the CIR can also be identified at 20:45 UT on February 14. Figure 2 depicts the criteria used to identify the SI (e.g., Jian et al. 2006; Richardson 2018), which include (a) an increase in the alpha/proton number density ratio; (b) a directional change in the tangential or normal component of the flow speed; (c) an increase in both alpha and proton temperature; (d) an abrupt increase in entropy (defined as $S = \ln(T_p^{3/2}/n_p)$), following an entropy dip and (e) the total proton pressure P reaches a maximum in the vicinity of the interface. We also identified an HCS crossing near the SI by directional change of the B_x component, as shown in the second panel of Figure 1. In the electron PAD panel (fifth panel in Figure 1), there is a clear signature associated with the abrupt change in direction of the magnetic field, the unidirectional electron beam initially aligned with the 180° pitch angle before the HCS crossing, and then the beam with a slightly larger intensity switched to 0° pitch angle after the HCS crossing. Simultaneously, around 02:30 UT on February 15, the interplanetary magnetic field (IMF) magnitude |B| decreases, and the proton density n_p increases, leading to a sharp increase in proton beta β_p (~10). These signatures indicate the HCS crossing (e.g., Zhao et al. 2021). However, it is not straightforward to distinguish the exact location of SI and HCS from the in situ measurements, and thus our further discussion is under the assumption that the SI and HCS (hereinafter SI+HCS) are mixed for this event.

Around February 18 00:49 UT, a ICME-driven fast-forward shock (hereinafter FS2) is observed that has been identified by several studies (Maričić et al. 2014; Mishra & Srivastava 2014). The sudden jump in the magnetic field strength from \sim 3.3 to \sim 15 nT, the velocity increases from \sim 350 to \sim 450 km s⁻¹, the proton density increases from \sim 7 to \sim 22 cm⁻³, and the proton

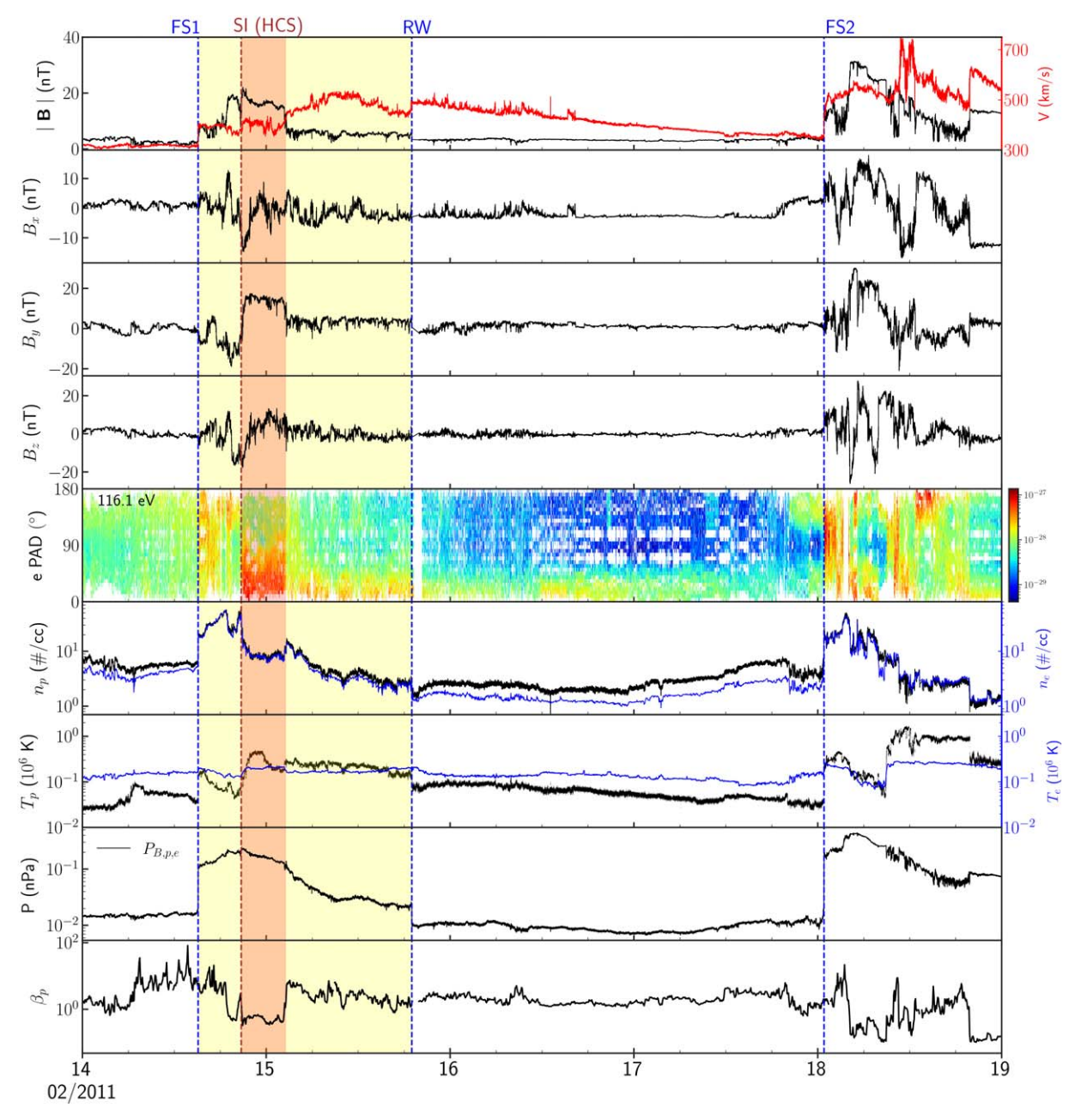


Figure 1. The panels from top to bottom show the magnitude of the magnetic field and the solar wind speed, the magnetic field components in the GSE coordinates, the electron PAD at 116.1 eV, the proton number density n_p , and the electron number density n_e , the proton temperature T_p and the electron temperature T_p and the electron temperature T_p , the total pressure calculated by the sum of magnetic pressure, thermal proton, and electron pressure P and the proton plasma β_p from 2011 February 14 00:00 UT–February 19 00:00 UT. The yellow-shaded region identifies the CIR structure. The three blue dashed vertical lines identify the location of a fast-forward shock (FS1), an RW, and an FS2. The SI is marked by the red-dashed vertical line. The red-shaded region highlights the mixing of SI and HCS crossings.

and electron temperature and total pressure correspondingly show a sharp increase, all correspond to FS2. Overall, this particular event lasting about 5 days from 2011 February 14 to 19, provides a great opportunity to study the behavior of energetic particles in a system of multiple shocks associated with different large-scale structures.

2.1. Shock Geometry and Parameters

In the following analysis, we focus on the CIR region bounded by the FS1-RW pair and in the vicinity of the FS2 observed by the WIND spacecraft. The shock normal is obtained by the mixed coplanarity method:

$$\hat{\mathbf{n}}_{MX1} = \pm \frac{(B_u \times \Delta V) \times \Delta B}{|(B_u \times \Delta V) \times \Delta B|},\tag{1}$$

where $\Delta \mathbf{B} = \mathbf{B}_d - \mathbf{B}_u$ and $\Delta \mathbf{V} = \mathbf{V}_d - \mathbf{V}_u$ are the IMF and solar wind speed changes, respectively, and the subscripts u and d denote the upstream and downstream values across the shocks.

In Table 1, the first eight rows from top to bottom list the shock normal \hat{n} components in GSE coordinate, shock obliquity $\theta_{\rm Bn}$, compression ratio $(r=n_{pd}/n_{\rm pu})$, Alfvén Mach number $M_{\rm A}$, shock speed $V_{\rm sh}$, and upstream proton plasma beta

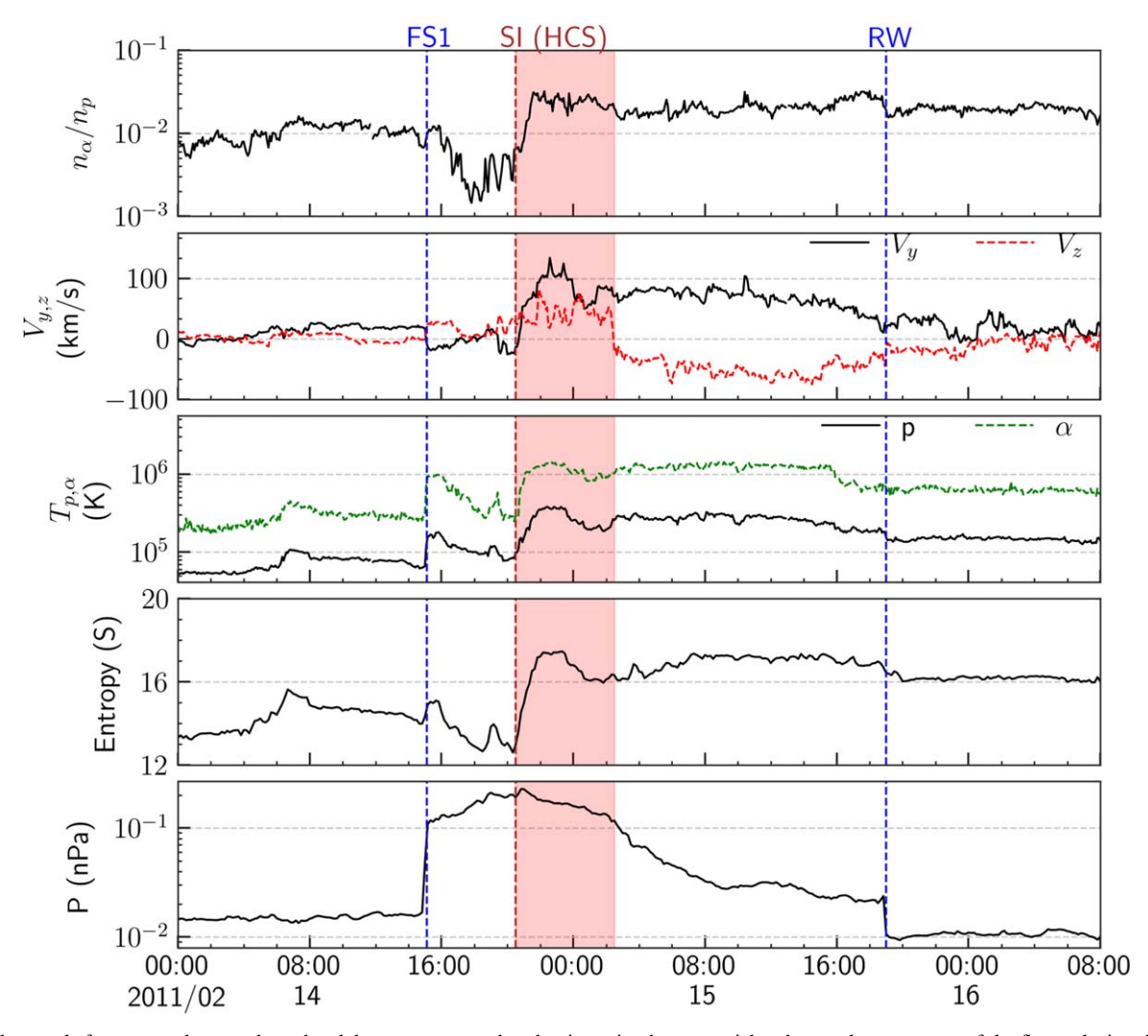


Figure 2. The panels from top to bottom show the alpha to proton number density ratio, the tangential and normal components of the flow velocity, the alpha and proton temperature, the entropy, and the total pressure from 2011 February 14 00:00 UT–February 16 08:00 UT. The CIR interval is bounded by two blue vertical dashed lines, while a red-dashed vertical line denotes the SI and the start of the HCS crossing.

 β_{pu} , calculated from WIND in situ measurements for FS1, RW, and FS2. The last row in Table 1 lists the upstream and downstream intervals chosen for calculating the mean values for FS1, RW, and FS2, respectively. The shock normal direction is a long-standing challenge for single-point observations and depends strongly on the method of calculation and the length of the interval chosen. Even if the Rankine-Hugoniot conditions are used to constrain the calculation of the shock normal direction, there remains the question of whether firstorder fluctuations should be considered in the MHD equations. Since the remaining shock parameters are based on the shock normal, the parameters for FS1 and FS2 listed in Table 1 are within a certain uncertainty range, which is obtained from the CfA Interplanetary Shock Database. For the RW, since it does not steepen into a shock wave, it is difficult to determine the shock parameters. Therefore, we provide only approximate estimates of these parameters based on the average background field and plasma parameters over selected upstream and downstream intervals. As shown in the table, FS1 and FS2 are quasi-perpendicular shocks, and the RW has a quasiparallel geometry with a relatively low compression ratio and Mach number. The shock speed of all three shock/waves are similar and less than 500 km s⁻¹. In general, particles are more

likely to be accelerated at quasi-parallel shocks because the particles will more easily cross the shock wave multiple times along the field lines to obtain the acceleration. Quasi-parallel shocks are able to excite upstream waves via a streaming instability with greater efficiency than quasi-perpendicular shocks (Bell 1978; Lee 1983; Gordon et al. 1999; Zank et al. 2000; Rice et al. 2003; Zank et al. 2006). The upstream excited waves can trap the particles around the shock thereby preventing upstream escape and thus leading to the particles crossing the shock repeatedly. The diffusive shock acceleration (DSA) process is therefore expected to work best at quasiparallel shocks. When the shock becomes more oblique, because of its magnetic field and shock normal geometry, quasi-perpendicular shocks can effectively trap particles in the vicinity of the shock without generating waves, aided by the large-scale preexisting turbulence through which the shock moves. An increasing fraction of the reflected particles will be unable to escape and will be convected into the downstream region and thermalized. This is the reason why the injection energy into the diffusive acceleration process is expected to increase with increasing shock angle. In a more general case with an oblique or quasi-perpendicular shock, shock drift acceleration (SDA) takes place. Particles drift along the shock

Table 1
Shock Parameters Derived from WIND Observations

Parameters	FS1	RW	FS2
Shock normal <i>x</i> -component, \hat{n}_x	-0.86 ± 0.03	-0.88	-0.82 ± 0.02
Shock normal y-component, \hat{n}_y	-0.45 ± 0.01	0.19	0.20 ± 0.03
Shock normal z-component, \hat{n}_z	0.22 ± 0.02	0.45	0.52 ± 0.02
Shock angle, θ_{Bn} (degrees)	$78^{\circ} \pm 4.2$	8°16	$79^{\circ} \pm 4.4$
Compression ratio, r	3.08 ± 0.12	1.65	3.01 ± 0.14
Alfvén Mach number, M _A	5.70 ± 1.36	1.02	4.98 ± 1.20
Shock speed, $V_{\rm sh}$ (km s ⁻¹)	391 ± 4.2	400	462 ± 7.9
Upstream proton plasma beta, β_{pu}	4.34 ± 0.25	2.47	1.11 ± 0.26
Chosen intervals	Upstream: 14:57–15:05 UT, Feb 14 Downstream: 15:08–15:16 UT, Feb 14	19:01–19:09 UT, Feb 15 18:50–18:58 UT, Feb 15	00:39–00:47 UT, Feb 18 00:55–01:03 UT, Feb 18

front and get accelerated by the convective electric field $(E = -u_1 \times B_1)$ parallel to the drift motion (Armstrong & Decker 1979; Jokipii 1982; Decker & Vlahos 1986). Jokipii (1982) and Zank et al. (2006) pointed out that SDA can be incorporated into DSA when particle scattering is included in SDA, i.e., the individual particle energy gain proceeds through SDA, but repeated scattering downstream of the quasiperpendicular shock can ensure the return of the particles to the shock front. This causes quasi-perpendicular shocks to accelerate particles faster and to higher energies. There is hence a theoretical distinction between (1) fast acceleration to high energies at quasi-perpendicular shocks, out of a suprathermal seed population, and (2) slower acceleration to lower energies at quasi-parallel shocks, which can accelerate ions out of the thermal background. The standard equilibrium shock acceleration theory predicts a power-law distribution function $f(p) \sim p^{-\alpha}$, where $\alpha = \frac{3r}{r-1}$ is the energy spectral index with r the shock compression ratio.

2.2. Energetic Particle Profile

As shown by Figures 3(a) (protons), (b) (electrons), and (c) (helium), the CIR is preceded by a quiet period without any increase in the intensity of energetic particles.

Using Equation (A2), we calculate the threshold injection energy of protons and helium and find that the energy range of the studied ions exceeds the threshold injection energy and can be accelerated at FS1. However, for electrons, we cannot use Equation (A2) to estimate the threshold injection energy because the parallel and perpendicular mean free paths shown in Equations (A3) and (A4) are based on the assumption of magnetostatic turbulence and a spectrum without dissipation range. This assumption does not apply to low-energy electrons because they resonate with the dissipation range turbulence. Furthermore, the mean free paths of electrons and ions can differ fundamentally (Bieber et al. 1994). Electrons with the same rigidity as protons can have a larger mean free path, indicating that the mean free path has an explicit speed dependence. This can lead to very different injection challenges for electrons and protons (Amano et al. 2022). The basic idea of DSA theory was proven by spacecraft measurements of energetic ions around Earth's bow shock as well as IP shocks driven by CMEs (e.g., Lee 1983; Kennel et al. 1986). However, why these shocks are relatively weak in electron acceleration or heating relative to ions is still not fully understood. In recent years, many possible electron acceleration mechanisms for collisionless shocks have been noted (Amano et al. 2022). But how the acceleration efficiency depends on the shock

parameters (e.g., Mach number, shock obliquity) remains unclear. In this section, we will focus on individual species and try to understand how they are accelerated in CIR- and ICME-driven shocks.

As seen from Figure 3(a), low-energy protons (210–550 keV) show flux enhancement at FS1, followed by a decrease in intensity to the pre-enhancement level before SI, a phenomenon that occurs only in low-energy protons and may be related to the DSA process at FS1. Interestingly, the low-energy protons then exhibit a local peak in the SI+HCS region (red-shaded area). One possible explanation is that the low-energy protons experience local compression acceleration at the SI+HCS (e.g., Wei et al. 2022). At the trailing edge of the CIR, the intensity of energetic protons begin to increase over all energy ranges (210-4.40 MeV). Significant flux enhancement is observed, especially for protons at the higher-energy range, which are not accelerated at FS1 and SI +HCS. The characteristic that the flux increase of high-energy protons is more significant than that of low-energy protons is consistent with the prediction of magnetic reconnection-related local acceleration theory previously applied to the CIR particles (Khabarova et al. 2015, 2016; Zhao et al. 2018b, 2019). Rather remarkably, Zhao et al. (2018b) chose a particle injection point close to HCS and successfully reproduced the observed energetic particle "time-intensity" profile and energy spectra using the stochastic acceleration theory of multiple interacting magnetic islands. Here, we do not address the theoretical predictions but focus exclusively on the interpretation of plasma and field properties.

Upstream of the RW (i.e., after 19:00 UT on February 15), the intensity of high-energy ions experiences an exponential decay. The RW, as a quasi-parallel shock, has a simple injection criterion: a particle must possess a speed (v) at least comparable to the upstream flow speed (u_1) to diffuse or propagate from downstream of the shock into the upstream region, as outlined in Equation (A1). As the particle diffuses repeatedly across the shock front, it undergoes identical head-on collisions with scattering centers in the upstream and downstream flows, resulting in a net energy gain. Consequently, one can anticipate an efficient acceleration process at the quasi-parallel RW. Compression due to the CIR together with the HCS crossing provides favorable conditions for particle energization. It is not clear, however, whether it is the preexisting population of energetic particles or the fact that the later RW moves through a more (magnetically) turbulent medium, which increases the trapping of the particles, leading to a higher acceleration rate. After crossing the RW, the particle intensity is expected to gradually weaken over time as particles are dispersed and undergo cooling in the expanding solar

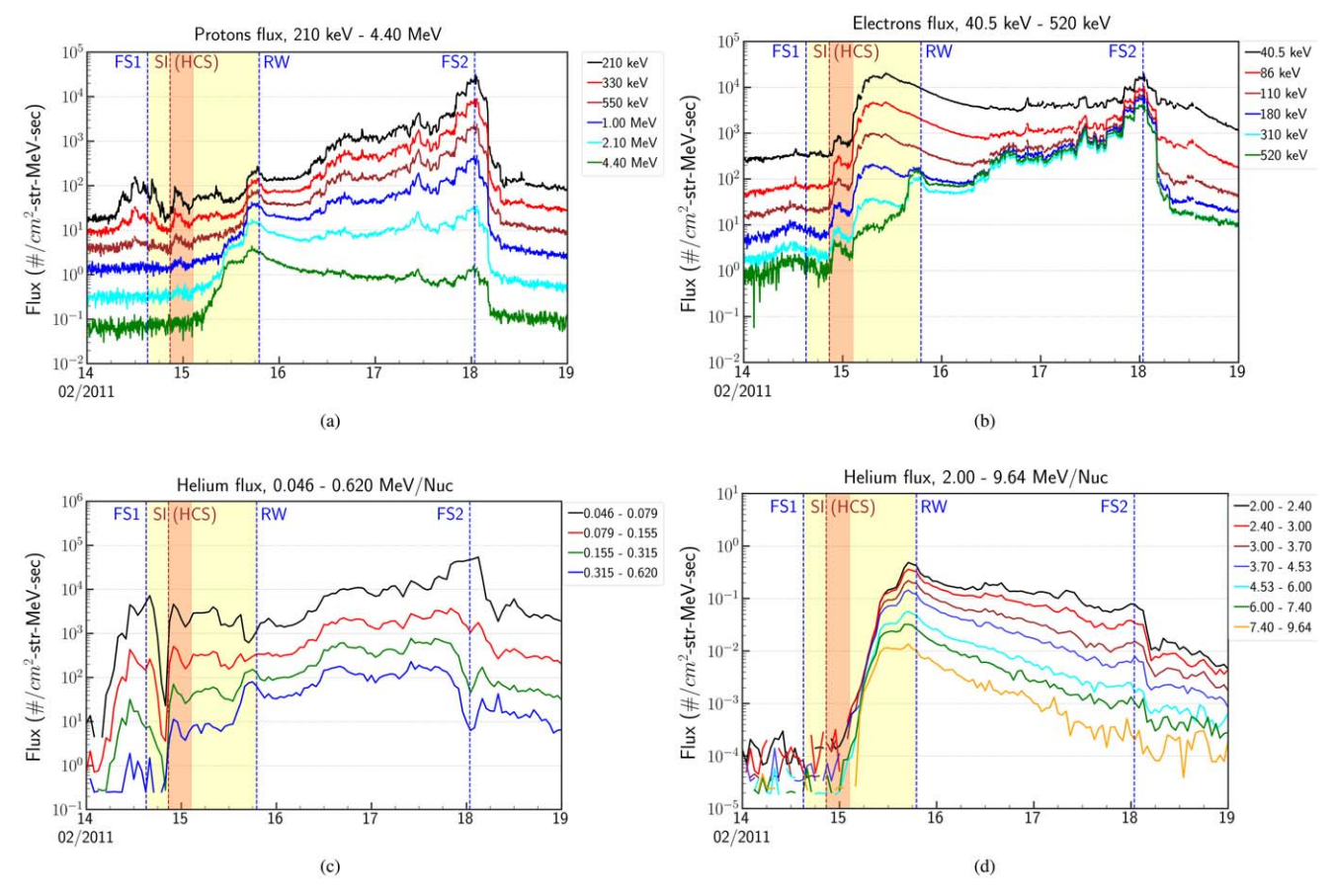


Figure 3. Five minute averages of (a) the 0.21–4.40 MeV proton intensities (b) the 40.5–520 keV electron intensities from WIND 3DP, (c) hourly averages of the 0.046–0.620 MeV nuc⁻¹ helium intensities from WIND EPACT/STEP, and (d) hourly averages of the 2.00–9.64 MeV nuc⁻¹ helium intensities from WIND EPACT/LEMT at multiple shocks. FS1 and RW correspond to the shocks driven by the CIR structure, and FS2 corresponds to the ICME-driven shock. The yellow-shaded region indicates the in situ observation of the CIR region and the red-shaded region corresponds to SI+HCS.

wind (Zank et al. 2000). However, the occurrence of the CMEdriven fast-forward shock FS2 on February 18, 00:49 UT led to another increase in energetic particle intensities, particularly notable for ions (\$\leq 1 \text{ MeV nuc}^{-1}\right) and high-energy electrons. For instance, at the lowest energy channel of 210 keV protons (see Figure 3(a)), the flux increases by more than 2 orders of magnitude. One possible explanation is that the combined effect of shock, and SI+HCS structure associated with the CIR significantly enhances proton acceleration at the subsequent CME-driven shock, particularly if the acceleration process is not yet complete. This means that the particles have not yet reached their maximum possible momentum during the acceleration process at the CIR-associated shock/waves. These particles retain the potential to gain additional momentum and further be accelerated when encountering subsequent shocks. This sustained ability to accelerate highlights key dynamics in particle behavior during multiple shock events. Previous studies have also shown that the combined effects of multiple shocks and reacceleration can make the overall acceleration process more efficient compared to a single shock scenario (e.g., Melrose & Pope 1993). Remarkably, Parker & Zank (2014) modeled the behavior of diffusively accelerated particles at multiple shocks with different characteristics and showed that the previous particle distribution plays an important role in the final particle distribution, assuming the dynamical timescale between shocks is sufficiently short to allow for the contributions from the previously accelerated distribution. Specifically, they found that the energy spectrum of particles accelerated in a sequence of shock waves tends to be flatter compared to the distribution of particles accelerated by a single shock wave. However, we note that the multiple shock scenario proposed by Parker & Zank (2014) is more suitable for multiple CME-driven shocks, where the dynamical timescale of the shock is appropriate to an expanding blast wave initiated near the solar surface. The CIR shocks (FS1 and RW) investigated here are driven by the overtaking fast wind plowing into the solar wind, so the dynamical form of the interaction is different from that of a blast wave. It is also noteworthy that both FS1 and FS2 are quasi-perpendicular shocks with similar density compression and shock normal angle. Nevertheless, FS2 is found to accelerate low-energy protons more efficiently compared to FS1. This concludes that the suprathermal particles may serve as "seed" particles for the mechanism by which particles accelerate to higher energies at the shock waves driven by CMEs (Thomsen 1985; Mason 2000).

On the other hand, the electron flux with varying energies behaves differently. At the forward shock FS1, only higher-energy electrons (180–520 keV) undergo weak acceleration. A long-standing problem with the DSA of electrons is the difficulty in resonantly scattering electrons of moderate energy—only already energetic electrons can scatter off the waves excited by the streaming instability at a shock (Lee 1983). Thus, low-energy electrons are difficult to be accelerated by the DSA process. Nevertheless, Amano et al. (2022) provide a potential solution to this problem. They argue that DSA can be

effective for low-energy electrons that traverse the shock wave in a completely adiabatic manner, as long as the particles are subject to pitch angle scattering both upstream and downstream. At the SI+HCS, the electrons in all the energy ranges show a local peak, which was also seen for low-energy protons, as discussed earlier. Crooker et al. (2010) also found that the suprathermal electron flux peaks around or right at the interface by investigating SIRs via the WIND observation. The most notable aspect of Figure 3(b) is that energetic electrons show significant enhancement immediately after SI+HCS, especially for the 40.5-180 keV energy range. We suspect that local acceleration may occur near the HCS, possibly due to magnetic island-related reconnection acceleration (Zank et al. 2014; Le Roux et al. 2016; Du et al. 2020; Li et al. 2021). At the RW, it is interesting to note that only high-energy electrons (310–520 keV) get accelerated, which is similar to high-energy ions. As discussed earlier at FS1, electrons can be efficiently accelerated at a shock via the DSA mechanism if they are energetic enough and can experience pitch angle scattering both upstream and downstream of the shock. This feature can also be seen at later CME-driven shock FS2, where the enhancement of the high-energy electron flux is almost 2 orders of magnitude greater than the minimum flux right after the RW around February 16 06:00 UT.

Furthermore, for helium particles, as shown in Figure 3(c), the time-intensity profiles of low-energy helium first show strong enhancement at FS1, followed by an abrupt decrease in the region between FS1 and SI, and then again increase immediately at the boundary of SI+HCS boundary. This behavior is different from high-energy helium, shown in Figure 3(d), as helium flux at both FS1 and SI seems quiet without any flux enhancement. But, the high-energy helium flux also starts to increase at the boundary of SI+HCS for all energy channels (2.00–9.64 MeV nuc⁻¹) and peaks sharply in the vicinity of the RW, which is consistent with high-energy proton profiles shown in panel (a). On the other hand, the lowenergy helium flux (0.046–0.155 MeV nuc⁻¹) does not show enhancement at the RW because its energy is below the injection threshold at a quasi-parallel shock, as explained in Equation (A1). After crossing the RW, the low-energy helium flux starts to increase, which shows that the low-energy helium can also be accelerated at FS2, behaving like low-energy protons. Additionally, we note that compared to protons of the same energy, the helium flux decreases faster after passing through the CIR structure and is barely accelerated at the FS2 shock front. A possible explanation is that it may be possible that helium is preferentially accelerated at the RW. One of the most relevant aspects is the ion heating process in the solar wind, which has been proven that the heavy ions are preferentially heated and accelerated with respect to protons via wave-particle interactions and stochastic ion heating (e.g., Isenberg & Vasquez 2009; Cranmer & Van Ballegooijen 2012). If the helium distribution is already saturated due to the acceleration at the RW, then they cannot be further accelerated unless the later shock FS2 is stronger. Energetic particles cannot be enhanced relative to themselves if the energization does not overcome the energy loss. On the other hand, there is not enough energy left for protons after helium and minor ions are accelerated at the CIR structure, leaving the proton acceleration stopped at the "seeding" stage, from which the later CME-driven shock picks up further proton acceleration. In other words, it is possible that helium is preferentially

accelerated at the preceding CIR shocks/waves if the acceleration of helium is more efficient than protons. The time-intensity profile shows that the helium flux of ~2 MeV nuc⁻¹ at the CIR RW increases by ~4 orders of magnitude compared to protons of similar energy, which only increase by less than 2 orders of magnitude. Therefore, it is reasonable that upstream of the later FS2 shock, the helium flux continues to decrease without any acceleration, while the protons can essentially maintain the same flux level or even accelerate further. By comparing our event to the isolated IP shocks without a preceding CIR structure (not shown here), we find further evidence that isolated shock events tend to show weaker proton acceleration and the helium flux enhancement is comparable to that of protons of the same energy, suggesting that preacceleration at the CIR contributes to proton acceleration at the later shock FS2.

3. Turbulence Properties within the CIR Structure

Turbulence within the CIR can play a crucial role in the DSA process. The enhanced turbulence and wave activity prevalent downstream of CIR reverse shocks compared to forward shocks (Tsurutani et al. 1995) may lead to a more efficient acceleration of particles near the trailing edge (Schwadron et al. 1996). Also, the preexisting fluctuations are particularly important for the acceleration of particles at quasi-perpendicular shocks (Guo et al. 2021). It is therefore useful to analyze magnetic field fluctuations within the CIR structure.

We carry out a power spectral density (PSD) analysis of the magnetic field fluctuations using 92 ms resolution of WIND magnetic field measurements from 2011 February 14 10:45 UT–February 16 00:45 UT. The analysis is based on the Fourier-transformed autocorrelation tensor of the magnetic field components, from which the total PSD is taken as its trace spectrum. (Leamon et al. 1998), i.e.,

$$PSD = \mathcal{F}[b_x b_x' + b_y b_y' + b_z b_z'], \tag{2}$$

where \mathcal{F} denotes the Fourier transformation and b_x b_x' , b_y b_y' , and b_z b_z' are the autocorrelation functions of the fluctuations in three magnetic field components, respectively. The solid lines are the power spectra corresponding to different regions within the CIR structure, and they are color-coded by the time in hours from the SI and normalized by the time of the RW. Each power spectrum is calculated in a nonoverlapping $2\,\mathrm{hr}$ sliding window. A Kolmogorov-like $f^{-5/3}$ spectrum is displayed for reference. The trace spectra P_{Tr} (right panel) are further decomposed into parallel P_{\parallel} (left panel) and perpendicular P_{\perp} (middle panel) fluctuations relative to the mean magnetic field direction in each 2 hr window. From Figure 4, it is evident that the magnetic field fluctuation intensity is clearly larger in the vicinity of SI+HCS followed by followed by the regions around the RW. The total magnetic fluctuation power is dominated by the incompressible transverse fluctuation P_{\perp} . The compressible parallel fluctuation P_{\parallel} is relatively small at every location. This may be important for the interpretation of the observed energetic particle enhancement within the CIR structure. Turbulence has a well-known effect on the scattering mean free path of the particle, thus affecting the efficiency of particle acceleration. Moreover, turbulence may also play a more direct role in particle acceleration. For example, magnetic

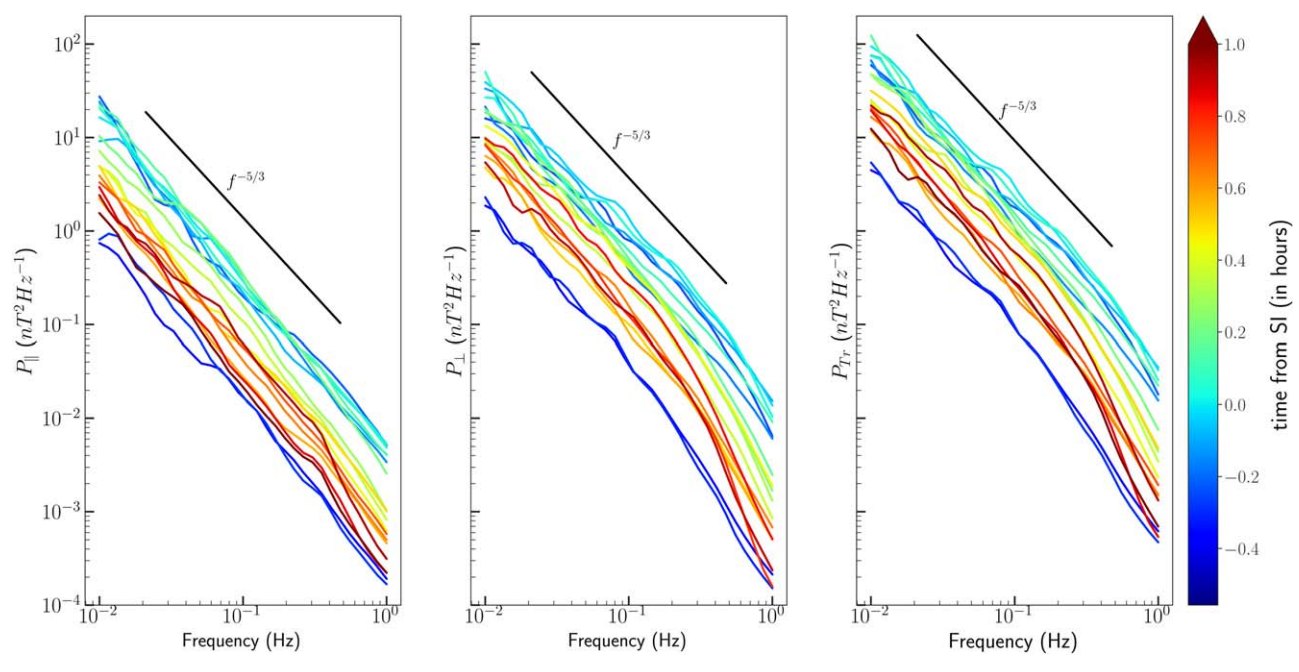


Figure 4. A typical nonoverlapping sliding window PSD analysis of the magnetic field fluctuations for the FS1-RW pair. The panels from left to right plot the compressible parallel fluctuations (P_{\parallel}), incompressible transverse fluctuations (P_{\perp}) and total magnetic field fluctuations (P_{Tr}). The color bar is the time from SI (in hours) normalized by the far downstream time of the RW. A Kolmogorov-like $f^{-5/3}$ spectrum is displayed for reference.

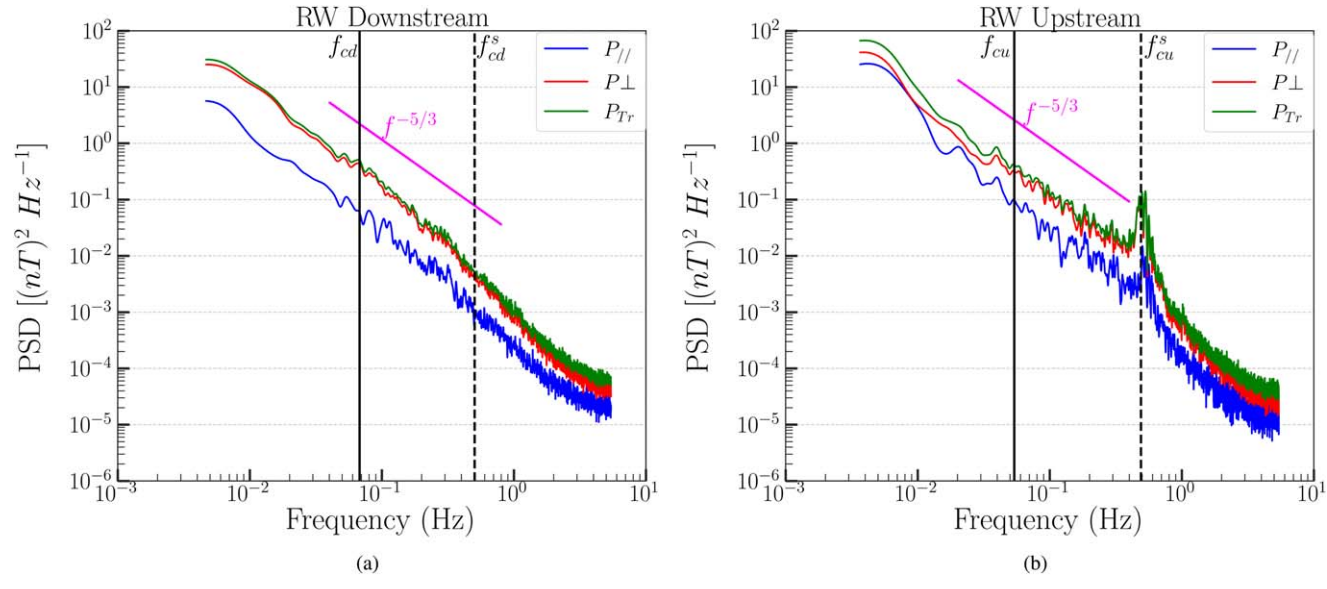


Figure 5. Power spectra for the total trace magnetic field fluctuations (P_{Tr}) , parallel (P_{\parallel}) , and transverse fluctuations (P_{\perp}) (a) upstream (February 15 18:00 UT–18:50 UT) and (b) downstream (February 15 19:10 UT–20:00 UT) of the RW. The vertical lines correspond to the proton gyrofrequencies in the plasma frame (solid line) and spacecraft frame (dashed line). A Kolmogorov-like $f^{-5/3}$ spectrum is displayed for reference.

island-like turbulence is often accompanied by magnetic reconnection through their dynamic interaction and can lead to particle acceleration (e.g., Zank et al. 2014; Zhao et al. 2018b). From Figure 4, it is noteworthy to observe the spectral bump occurring in the vicinity of the RW (red solid lines), prompting a closer look into the PSD of magnetic field fluctuations within this domain.

We select about 1 hr time intervals for regions both downstream (18:00 UT–18:50 UT) and upstream (19:10 UT–20:00 UT) regions of the RW and plot the magnetic field power spectrum using the Welch method as shown in Figure 5. As a reference, the proton cyclotron frequencies in the plasma frame

are plotted both upstream $(f_{\rm cu})$ and downstream $(f_{\rm cd})$ and the equivalent frequencies in the spacecraft frame $f_{\rm cu}^s = f_{\rm cu} \times V_{\rm sw,u}/V_{\rm A,u}$ and $f_{\rm cd}^s = f_{\rm cd} \times V_{\rm sw,d}/V_{\rm A,d}$ is also shown. Here, $V_{\rm sw}$ and $V_{\rm A}$ are the solar wind and Alfvén speed estimated by plasma measurements. The black solid lines correspond to $f_{\rm cu}^s$ and $f_{\rm cd}^s$ and the black dotted lines correspond to $f_{\rm cu}^s$ and $f_{\rm cd}^s$. We performed a power-law fitting in the inertial range and found a Kolmogorov-like $(f^{-5/3})$ spectrum upstream and a steeper spectrum downstream of the RW. The power spectra show some flattening at high frequencies, which may be attributed to instrumental noise (Woodham et al. 2018; Pitňa et al. 2021). It is also evident that the transverse fluctuations dominate,

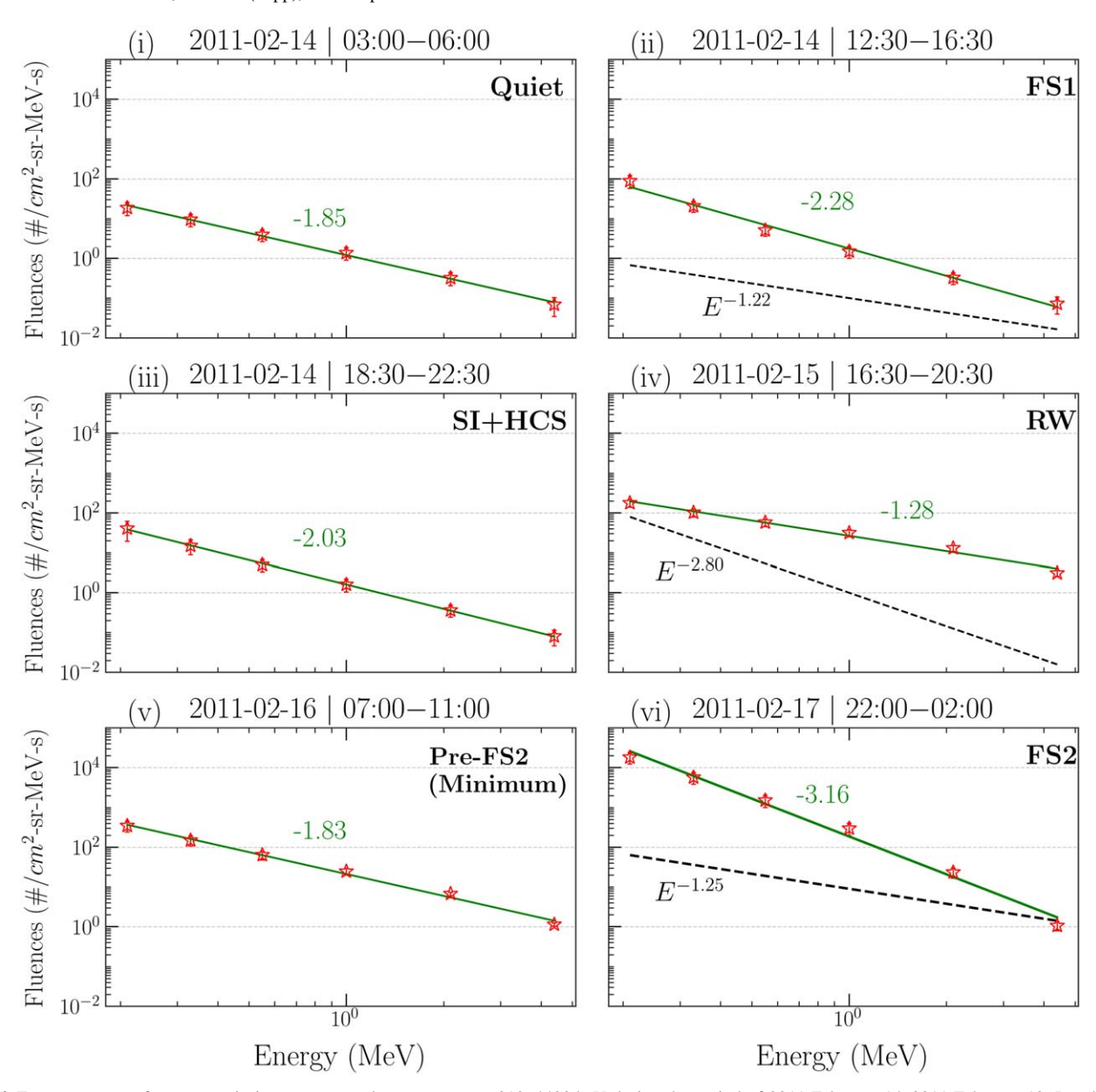


Figure 6. Energy spectra of proton at six instances over the energy range 210–4400 keV during the period of 2011 February 14–2011 February 19. Panels (i)–(vi) show, in chronological order, the spectrum at (a) quiet time; (b) the forward shock (FS1); (c) the SI mixed with HCS; (d) the RW; (e) pre-FS2 (the intensity begins to increase), and (f) the forward shock (FS2). A power-law fit (green solid line) is applied when the spectrum exhibits a power-law shape, and the resulting spectral index is shown in green text. The 1D standard DSA spectrum (black dashed lines) based on the observed compression ratio for each shock is shown for reference.

indicating the prevalence of nearly incompressible fluctuations (Zank et al. 2017). We also find that the power spectrum just upstream of the RW has a bump near the proton gyrofrequency (~0.5 Hz), which indicates ion-scale wave activity. Since the spectral bumps mainly exist in incompressible transverse fluctuations, we suspect that the enhanced power at the proton gyrofrequency may be related to an ion cyclotron wave. For quasi-parallel shocks like the RW in our case, the turbulence (mainly incompressible Alfvén waves or structures) may be generated by the anisotropic energetic protons at the shock (Lee 1983).

4. Evolution of the Energetic Particle Spectrum

To study the spectral variations, we choose several regions inside and outside the CIR for further analysis. Panel (i) of Figure 6 and panel (a) of Figure 7 illustrates proton energy

spectra and velocity distribution function (VDF) before the CIR, marked as "quiet." We selected 3 hr (February 14 03:00 UT–06:00 UT) averaged flux for the quiet-time period. The energy spectra and VDFs for the other regions are shown in Figure 6, panels (ii)–(vi) and Figure 7, panels (b)–(f), respectively. We use 4 hr averaged fluxes for these regions. Since the flux data are not always available, we consider only six energy channels of protons (210 keV–4.4 MeV) during the period of averaging.

Figure 6 panels (i)—(vi) show the proton energy spectra at six representative instances, which are organized in chronological order. Panel (i) shows that the quiet-time proton spectrum exhibits a typical power-law shape with an energy spectral index of -1.85. Panel (ii) shows that at the CIR-associated FS1 arrival time, the low-energy particle intensity is slightly enhanced, and hence, the spectrum becomes steeper compared

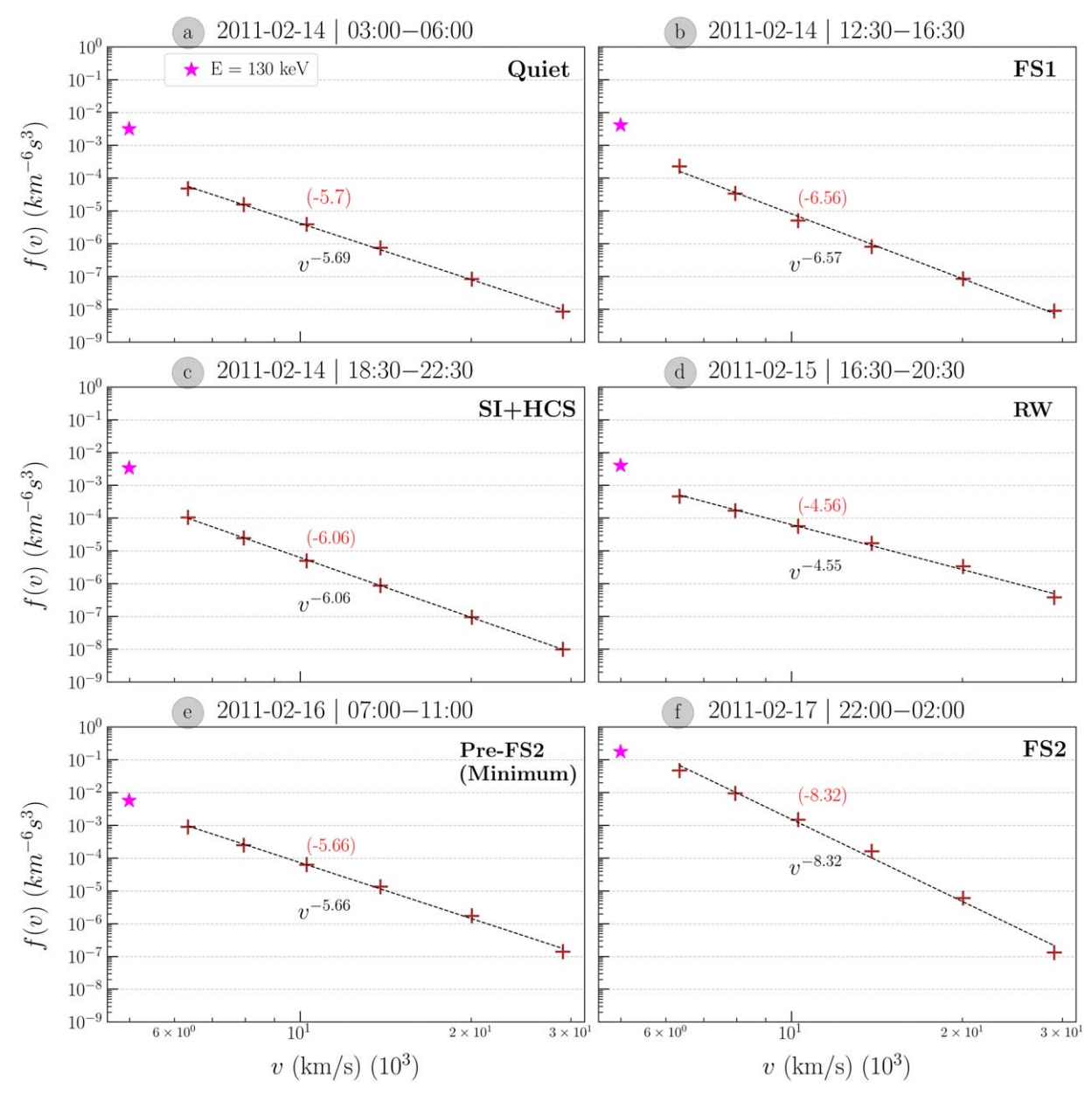


Figure 7. VDFs for protons in the energy range 130–4400 keV. Panels (a)–(f) show the VDFs at the same six instances as shown in the energy spectra. The magenta star corresponds to the proton with an energy of 130 keV. The dashed black line indicates the power-law fit to the VDF and and the fitted VDF power-law index is shown in black text. The indices shown in red are those derived from the energy spectra fit shown in Figure 6.

to the quiet-time spectrum. After the FS1, in the vicinity of the SI+HCS region, only the low-energy proton flux (<1 MeV) decreases a bit, while the high-energy particles remain at the same level. Therefore, we can expect a spectrum resembling that of panel (ii). At the trailing edge of the SI+HCS boundary, the proton fluxes start to increase in all the energy channels and are strongly enhanced at the RW, especially in the higherenergy channel (>330 keV). We find that the energy spectrum at the RW is harder than the DSA predicted spectrum. The strong enhancement of the high-energy proton flux and the hardening of the spectrum indicates that the energization of protons in the region between SI+HCS and RW may not be directly related to the DSA process. Outside the CIR region, it might be expected that the particle intensity would gradually decrease and return to a quiet level. Panel (v) illustrates that the proton activity has returned to the quiet level with a spectrum

resembling panel (i). Proton fluxes start increasing again on February 17 by the ICME-driven shock FS2, especially for the low-energy channels (210 keV-1 MeV), as shown by the change of power-law index from -1.83 to -3.16 in panel (vi). While FS2 represents a quasi-perpendicular shock, the acceleration process is significantly favored due to the preceding shock, RW. To understand whether the significant increase in low-energy proton flux at FS2 arises from a preexisting energetic source or a lower-energy source in the thermal solar wind, we generate plot proton VDFs shown in panels (a)-(f) of Figure 7. Notably, an additional energy channel (E = 130 keV) is included in this analysis. We convert the particle differential intensity, j(E), to the VDF, f(v), using, j $(E) = \frac{2E}{m^2} f(v)$ (Zhao et al. 2018b), where E is the particle energy and v'' is the particle speed. From the VDF plot depicted in Figure 7 panels (e) and (f), it is observed that the VDF of protons at energies below 200 keV, before the arrival of forward shock FS2, increases by more than 1 order of magnitude (magenta marker, corresponding to E = 130 keV). This suggests that the \sim 200 keV protons are presumably accelerated from the pool of lower-energy ions. However, the VDF of 130 keV proton shows no obvious increase within the CIR region, suggesting that the accelerated low-energy protons at the CME-driven shock may not come from preaccelerated particles at the CIR. Nevertheless, due to the absence of other lower-energy particles in the suprathermal energy range (e.g., below 100 keV), we cannot rule out the possibility of a preexisting energetic source produced by the preceding CIR structure, especially when the RW ($M_A = 1.02$) of the CIR is not sufficient enough to completely accelerate these particles. Also, Guo et al. (2021) mentioned that if the preexisting source has a much harder spectrum than that from the acceleration at the shock, the resulting distribution downstream of the shock retains the spectral index of the source spectrum, but that the intensity gets boosted across the shock. Comparing the proton energy spectrum in Figure 6 panels (v) and (vi), it can be seen that the resulting distribution downstream of the FS2 retains the spectral index of the source spectrum, i.e., proton energy spectrum has a similar spectral index to the source spectrum around 11:00 UT on February 16. From these two possible aspects, it is possible to explain that FS2-accelerated ion distribution in this event is related to the preexisting particles generated by the preceding CIR structure.

Figure 8 shows the corresponding energy spectra for electrons at six selected respective regions. It is seen that the quiet-time spectrum roughly follows a power-law with a spectral index of -2.2. Panel (ii) shows that at the FS1 arrival time, the spectrum does not change much and the electron fluxes are similar to the background level in all energy channels. The best-fit power-law index is calculated to be -2.17, which deviates significantly from the 1D standard DSA prediction $(E^{-1.22})$. This is also found in the proton energy spectra at all three shocks/waves. The exact reason for this deviation is unclear. It may be related to the intervals we choose when calculating the compression ratio. However, the most likely reason may be that DSA is ineffective at quasiperpendicular shocks. For quasi-parallel RW, the enhancement of high-energy ions may be due to compression-based reconnection acceleration. Panel (iii) illustrates that the spectrum becomes slightly steeper compared to panels (i) and (ii), which is related to the enhancement of low-energy electrons at the SI+HCS region. After crossing the SI+HCS region, we observed a significant enhancement of electron fluxes in all the energy channels. For example, panel (iv) shows the spectrum near the RW, where there is a significant increase in high-energy electron flux, resulting in a harder spectrum. As discussed in Section 2.2, the lower-energy electrons (40.5-180 keV) are accelerated at the SI+HCS boundary and are not further accelerated at the RW, whereas the higherenergy electrons (310-520 keV) get accelerated at both SI +HCS and especially near the RW. This suggests the acceleration seems to be more pronounced at the trailing edge or fast stream of the CIR structure compared to the FS1, which is consistent with the results of Richardson (2004) and Zhao et al. (2016). After crossing the CIR structure, the low-energy electron flux starts to decrease, and as it approaches FS2, the electron flux in >110 keV channels starts to increase, as shown by the flattening of spectrum in panel (v) and at FS2, the

electron fluxes in these energy channels are enhanced dramatically, especially for high-energy electrons. The best-fit power-law index is calculated to be -0.60, which is much harder than the spectra at the early two shocks. The strong enhancement of the electron flux and the hardening of the spectrum suggest that an IP shock in the presence of a preceding shock can significantly enhance the acceleration process for the electrons if they are energetic enough. Besides the seed particle intensity (Zank et al. 2000) and turbulence level (Li et al. 2003), shock geometry also plays an important role. Reames (2012) showed that a significant acceleration occurs for the quasi-perpendicular shock since shock drift may transfer a greater increment of energy each time a particle encounters the shock. However, Zank et al. (2006) have suggested that higher proton energies are achieved at quasiparallel rather than highly perpendicular shocks within 1 au, which has been reported in the recent findings (Battarbee et al. 2013; Afanasiev et al. 2018). A recent study by Ameri et al. (2023) analyzed energetic storm particle events in 116 IP shocks driven by CMEs and found no dependence between the energetic particle peak intensity and the shock normal angle. The results presented here have shown that acceleration is greatly favored at a quasi-perpendicular shock if multiple preceding shocks or any large-scale structures like CIR/SIRs are present. Nevertheless, a proper evaluation of the role of shock geometry on the acceleration process requires a more refined analysis that folds in time dependency as these parameters, such as θ_{Bn} or compression ratio r, may be strongly affected by local irregularities of the shock and variations in the plasma and magnetic field properties of the solar wind through which the shock is propagating (Lario et al. 2023). Additionally, when the separation time between the two shocks is small, the trapping effect between the two shocks may also contribute to the acceleration process.

5. PAD

In this section, we present the PAD of energetic particles by using eight pitch angle bins (ranging from $\sim 15^{\circ}$ to $\sim 165^{\circ}$).

Figure 9 shows the PAD of 180 keV electrons and 210 keV protons upstream and downstream of the CIR-associated RW. Both energetic electrons and protons have anisotropic PAD, as indicated by the peak in both downstream and upstream distributions being close to $\mu=1$. This suggests that the observed anisotropy is associated with field-aligned particles streaming from/at the vicinity of the shock. A form of DSA can be developed for an anisotropic distribution (Le Roux et al. 2007), but the reconnection-related local acceleration can also have an anisotropic PAD if it includes both the isotropic and the first-order anisotropy in the distribution function, which could account for the observed strong anisotropy shown here.

6. Conclusion

We analyze a CIR event that occurred on 2011 February 14–15, which comprised a pair of forward and reverse shocks and was followed by a CME-driven shock on February 18 00:49 UT. We investigate the acceleration of multiple particle species, including protons, electrons, and helium, at the three successive IP shocks by analyzing the particle energy spectra, VDF, turbulence, and PADs. The main results are summarized below

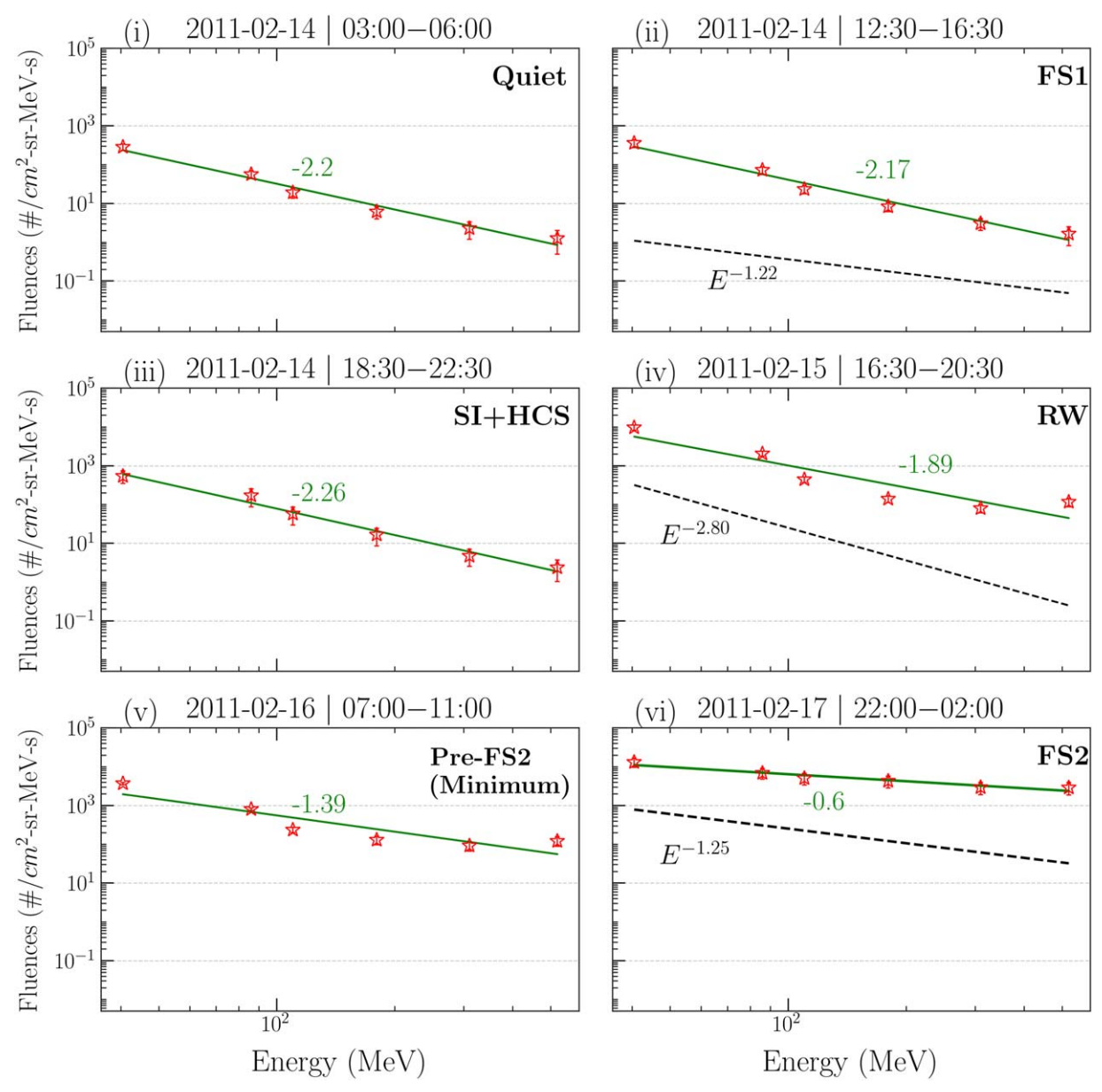


Figure 8. Energy spectra of electrons over the energy range 40.5–520 keV in the same format as Figure 6.

- 1. Near the leading edge (FS1) of the CIR, only the lowenergy protons within the energy range of 210 to 550 keV show a weak enhancement. A similar feature is observed near the SI for the protons of the same energy range. However, the electrons at low-energy bands (40.5-310 keV) show a significant enhancement near the SI+HCS, which is not observed upstream of FS1 and is probably due to the reconnection acceleration near the HCS. At the RW of the CIR, an enhancement is observed for ions at all energy ranges and for electrons within a certain energy range. The flux enhancement appears to depend on particle energy. The later ICME-driven fastforward shock FS2 has similar density compression and shock normal angle to that of CIR-associated forward shock FS1. By examining the lower-energy proton VDF and energy spectrum changes cross the FS2, we find that preexisting energetic protons generated by the preceding CIR may play an important role in the acceleration of
- low-energy protons at the subsequent perpendicular CME shock
- 2. Using a PSD analysis of the magnetic field fluctuations, we show that magnetic fluctuations are highly enhanced near the SI+HCS region, followed by the regions around the RW, which may be important in explaining the observed particle enhancement in the CIR trailing edge, suggesting that turbulence may play an important role in the observed acceleration between SI+HCS and RW. Nevertheless, this may be worth exploring in further detail. We also observed ion-scale wave activity near the proton gyrofrequency (spacecraft frame) in the upstream region of the reverse shock. Such increasing wave activity immediately upstream of the RW has also been reported in previous studies (Zank et al. 2006; Adhikari et al. 2016; Zhao et al. 2019). The resonant wave-particle interaction might be associated with the observed particle acceleration at the quasi-parallel RW.

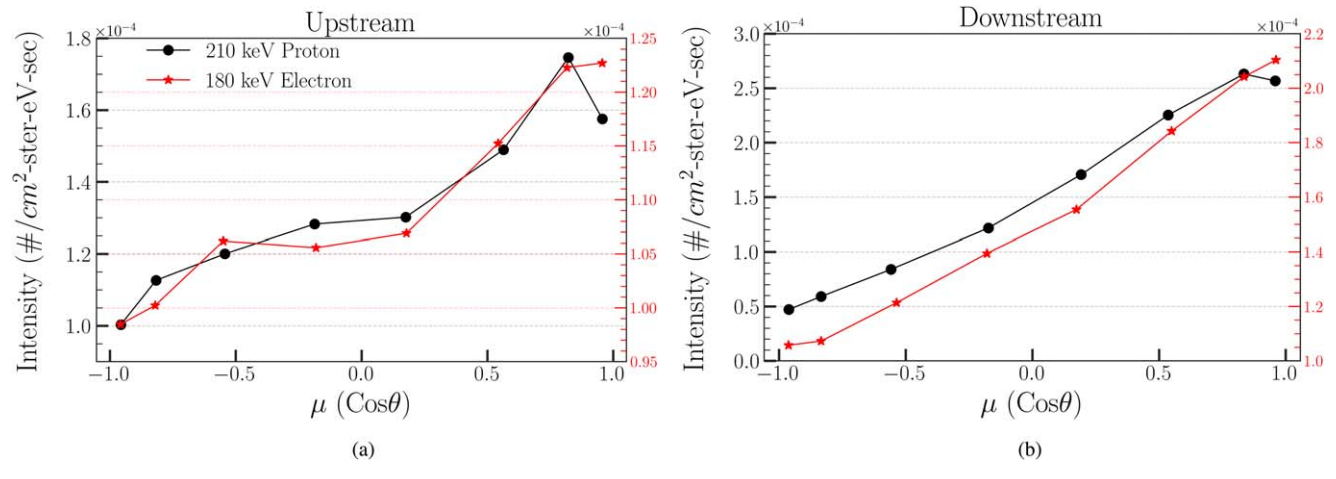


Figure 9. Pitch angle μ distribution of proton and electrons, (a) upstream (February 15, 14:50–18:50 UT) and (b) downstream (February 15, 19:10–23:10 UT) of the RW.

- 3. The energy spectra associated with the CIR event showed that there are no significant changes in the energy spectra observed at FS1 compared to the quiet-time spectrum, which suggests that the particles are not effectively accelerated at the forward shock FS1. However, after crossing the SI, which is further accompanied by HCS crossings, the spectra start to become flat (harder), and at the RW of the CIR structure, the spectra are much harder than DSA predicts. This suggests that the interaction of the HCS with shock/compressional waves may create favorable conditions for energy particle acceleration within CIR structures. Outside the CIR region, particle intensity is generally expected to decrease and return to quiet levels. The presence of FS2 greatly facilitates the subsequent energization process and leads to an increase in low-energy ions and high-energy electrons. However, since the VDF of low-energy protons (130 kev) does not show a significant increase in the CIR region, this seems to indicate that we cannot rule out another possibility, i.e., the protons at the CME shock that are accelerated by 2 orders of magnitude may be independent of the accelerated particles at the CIR.
- 4. The PAD of energetic protons and electrons exhibits strong anisotropy at the CIR-associated RW, suggesting that the observed anisotropy is associated with particles streaming from/at the vicinity of the shock.

Particle acceleration at solar wind events involving multiple shocks with a complicated morphology and global structure is not well understood theoretically or observationally. We analyze an interesting event of three closely spaced shocks/ waves associated with CIR and CME, respectively. One of the arguments for CIR particle acceleration in the inner heliosphere is whether the acceleration process requires the presence of a pair of well-defined and relatively strong shocks. From the studied event, this does not seem to be necessary. Flow compression can lead to acceleration, and the local reconnection-related acceleration mechanism seems promising to explain the energy dependence of the observed flux enhancement. A further study of energetic particles associated with CIRs using recent PSP and Solar Orbiter observations would potentially allow a more direct and in-depth comparison with 1 au observations.

Acknowledgments

We acknowledge the partial support of the NASA awards 80NSSC20K1783, 80NSSC23K0415, 80NSSC21K1319, a NASA PSP contract SV4-84017, an NSF EPSCoR RII-Track-1 Cooperative Agreement OIA-2148653, and a NASA IMAP sub-award under NASA contract 80GSFC19C0027. A.P. and B.P. acknowledge the partial support by the Czech Grant Agency under contract No. 23-06401S and the Charles University Grant Agency through project 280423. The authors acknowledge the use of WIND spacecraft data, publicly available at NASA/SPDF (https://cdaweb.gsfc.nasa.gov). We also acknowledge the use of the Interplanetary Shock Database via the Center for Astrophysics, Harvard University, USA (https://lweb.cfa. harvard.edu/shocks/wi_data/) and the University of Helsinki, Finland (http://www.ipshocks.fi).

Appendix The Injection Threshold at a Shock

For a quasi-parallel shock, the injection criteria require that the particle velocity should be at least comparable to the upstream plasma flow velocity,

$$v = u_1/\cos\theta_{\rm Bn},\tag{A1}$$

where v is the particle velocity, u_1 is the upstream plasma flow, and $\theta_{\rm Bn}$ is as previously defined (Lee 1983; Le Roux & Webb 2009). This is similar to the injection criteria introduced by Zank et al. (2000), who assumed that the injection energy is determined by the thermal energy downstream of the shock (with an injection efficiency of 1%). For particles to be accelerated diffusively at a quasi-perpendicular shock requires that they be sufficiently energetic already. According to Zank et al. (2006), the local injection momentum or velocity for particles to be accelerated diffusively at highly oblique shocks is

$$v_{\rm inj} = 3u \left[\frac{1}{(r-1)^2} + \frac{r_L^2 + \lambda_{\parallel}^2 \cos^2 \theta_{\rm Bn}}{(\lambda_{\perp} + \lambda_{\parallel} \cos^2 \theta_{\rm Bn})^2} \right]^{1/2}, \quad (A2)$$

where r_L is the Larmor radius, $\lambda_{\perp,\parallel}$ are the perpendicular and parallel mean free paths (related to the diffusion term, κ , by $\lambda = 3\kappa/\nu$). As described in Zank et al. (1998), the parallel

mean free path (λ_{\parallel}) based on standard quasi-linear theory and assuming magnetostatic turbulence is approximated by

$$\frac{\lambda_{\parallel}}{\lambda_{\text{slab}}} = 2.343 \frac{B_0^2}{\langle b_{\text{slab}}^2 \rangle} \left(\frac{r_L}{\lambda_{\text{slab}}} \right)^{\frac{1}{3}} (1+D), \tag{A3}$$

where
$$D = \frac{7A/9}{(m+1/3)(m+7/3)}$$
, $A = (1+n^2)^{5/6} - 1$, $n =$

where $D = \frac{7A/9}{(m+1/3)(m+7/3)}$, $A = (1+n^2)^{5/6} - 1$, $n = 0.746834 \ r_L/\lambda_c^{\rm slab}$ and $m = \frac{5n^2/3}{1+n^2-(1+n^2)^{1/6}}$. B_0 is the mean magnetic field strength, $\lambda_{\rm slab}$ is the slab correlation length and $\langle b_{\rm slab}^2 \rangle$ is the slab turbulence energy. Also, the perpendicular mean free path (λ_{\perp}) based on nonlinear guiding center theory is given by Zank et al. (2004)

$$\lambda_{\perp} = \left[\sqrt{3} \pi a^2 C \frac{\langle b_{\rm 2D}^2 \rangle}{B_0^2} \lambda_{\rm 2D} \right]^{2/3} \lambda_{\parallel}^{1/3},\tag{A4}$$

where $a^2=1/3$ is a factor related to the gyrocenter velocity, $C=\frac{\Gamma(\nu)}{2\sqrt{\pi}\Gamma(\nu-1/2)}$ is a constant such that $\nu=5/6$ yields a Kolmogorov spectrum. λ_{2D} is the 2D correlation length and $\langle b_{2D}^2 \rangle$ is the 2D turbulence energy.

For the calculation of the injection threshold, we assume that the ratio of the slab to 2D correlation scale is 2 (Pei et al. 2010; Chhiber et al. 2017; Zhao et al. 2017, 2018a). We also assume that the total energy in fluctuations can be divided into majority 2D and minority slab energies with the ratio, 80:20 (Zank & Matthaeus 1992, 1993; Bieber et al. 1996).

ORCID iDs

Ashok Silwal https://orcid.org/0000-0001-6286-2106 Lingling Zhao https://orcid.org/0000-0002-4299-0490 Gary P. Zank https://orcid.org/0000-0002-4642-6192 Bingbing Wang https://orcid.org/0000-0002-6000-1262 Alexander Pitña https://orcid.org/0000-0001-8913-191X Byeongseon Park https://orcid.org/0000-0002-7419-7999 Masaru Nakanotani https://orcid.org/0000-0002-7203-0730 Xingyu Zhu https://orcid.org/0000-0002-1541-6397

References

```
Adhikari, L., Zank, G., Hunana, P., & Hu, Q. 2016, ApJ, 833, 218
Afanasiev, A., Vainio, R., Rouillard, A. P., et al. 2018, A&A, 614, A4
Allen, R., Ho, G., Jian, L., et al. 2021, A&A, 650, A25
Allen, R., Lario, D., Odstrcil, D., et al. 2020, ApJS, 246, 36
Amano, T., Matsumoto, Y., Bohdan, A., et al. 2022, RvMPP, 6, 29
Ameri, D., Valtonen, E., Al-Sawad, A., & Vainio, R. 2023, AdSpR, 71, 2521
Armstrong, T., & Decker, R. 1979, in AIP Proc. 55, Particle Acceleration
  Mechanisms in Astrophysics, 101
Battarbee, M., Vainio, R., Laitinen, T., & Hietala, H. 2013, A&A, 558, A110
Belcher, J., & Davis, L., Jr. 1971, JGR, 76, 3534
Bell, A. 1978, MNRAS, 182, 147
Bieber, J. W., Matthaeus, W. H., Smith, C. W., et al. 1994, ApJ, 420, 294
Bieber, J. W., Wanner, W., & Matthaeus, W. H. 1996, JGRA, 101, 2511
Blandford, R. D., & Ostriker, J. P. 1978, ApJL, 221, L29
Cane, H., & Lario, D. 2006, SSRv, 123, 45
Chhiber, R., Subedi, P., Usmanov, A. V., et al. 2017, ApJS, 230, 21
Cranmer, S. R., & Van Ballegooijen, A. A. 2012, ApJ, 754, 92
Crooker, N., Appleton, E., Schwadron, N., & Owens, M. 2010, JGRA, 115,
Decker, R. B., & Vlahos, L. 1986, ApJ, 306, 710
Desai, M., Marsden, R., Sanderson, T., et al. 1999, JGRA, 104, 6705
Drury, L. O. 1983, RPPh, 46, 973
Du, S., Zank, G. P., Li, X., & Guo, F. 2020, PhRvE, 101, 033208
```

Ebert, R., Dayeh, M., Desai, M., & Mason, G. 2012, ApJ, 749, 73

```
Fisk, L., & Lee, M. 1980, ApJ, 237, 620
Giacalone, J., & Jokipii, J. 1997, GeoRL, 24, 1723
Giacalone, J., Jokipii, J., & Kóta, J. 2002, ApJ, 573, 845
Gloeckler, G., Hovestadt, D., & Fisk, L. 1979, ApJ Letters to the Editor,
  230, L191
Gordon, B., Lee, M., Möbius, E., & Trattner, K. 1999, JGRA, 104, 28263
Guo, F., Giacalone, J., & Zhao, L. 2021, FrASS, 8, 644354
Guo, F., Jokipii, J. R., & Kota, J. 2010, ApJ, 725, 128
Isenberg, P. A., & Vasquez, B. J. 2009, ApJ, 696, 591
Jian, L., Russell, C., & Luhmann, J. 2006, SoPh, 239, 337
Jian, L., Russell, C., Luhmann, J., & Skoug, R. 2008, SoPh, 249, 85
Jokipii, J. 1982, ApJ, 255, 716
Kennel, C., Coroniti, F., Scarf, F., et al. 1986, JGRA, 91, 11917
Khabarova, O., Zank, G., Li, G., et al. 2015, ApJ, 808, 181
Khabarova, O. V., Zank, G. P., Li, G., et al. 2016, ApJ, 827, 122
Krymskii, G. 1977, DoSSR, 234, 1306
Lario, D., Richardson, I., Aran, A., & Wijsen, N. 2023, ApJ, 950, 89
Le Roux, J., & Webb, G. 2009, ApJ, 693, 534
Le Roux, J., Webb, G., Florinski, V., & Zank, G. 2007, ApJ, 662, 350
Le Roux, J., Zank, G., Webb, G., & Khabarova, O. 2016, ApJ, 827, 47
Leamon, R. J., Smith, C. W., Ness, N. F., Matthaeus, W. H., & Wong, H. K.
   1998, JGRA, 103, 4775
Lee, M. A. 1983, JGRA, 88, 6109
Li, G. 2017, ScChD, 60, 1440
Li, G., Zank, G., & Rice, W. 2003, JGRA, 108, 1082
Li, X., Guo, F., & Liu, Y.-H. 2021, PhPl, 28, 052905
Maričić, D., Vršnak, B., Dumbović, M., et al. 2014, SoPh, 289, 351
Mason, G. 2000, American Institute of Physics Handbook (Melville, NY:
Mason, G., Mazur, J., Dwyer, J., Reames, D., & Von Rosenvinge, T. 1997,
   ApJL, 486, L149
McComas, D., Christian, E., Cohen, C., et al. 2019, Natur, 576, 223
McComas, D., & Schwadron, N. 2006, GeoRL, 33, L04102
Melrose, D., & Pope, M. 1993, PASA, 10, 222
Mewaldt, R., Stone, E., & Vogt, R. 1979, GeoRL, 6, 589
Mishra, W., & Srivastava, N. 2014, ApJ, 794, 64
Parker, L. N., & Zank, G. 2014, ApJ, 790, 153
Pei, C., Bieber, J., Breech, B., et al. 2010, JGRA, 115, A03103
Pitňa, A., Šafránková, J., Němeček, Z., Franci, L., & Pi, G. 2021, Atmos,
  12, 1547
Reames, D. V. 2012, ApJ, 757, 93
Rice, W., Zank, G., & Li, G. 2003, JGRA, 108, 1369
Richardson, I. 1985, P&SS, 33, 557
Richardson, I., Barbier, L., Reames, D., & Von Rosenvinge, T. 1993, JGRA,
  98. 13
Richardson, I. G. 2004, SSRv, 111, 267
Richardson, I. G. 2018, LRSP, 15, 1
Schwadron, N., Fisk, L., & Gloeckler, G. 1996, GeoRL, 23, 2871
Schwadron, N., Joyce, C., Aly, A., et al. 2021, A&A, 650, A24
Sokolov, I., Roussev, I., Fisk, L., et al. 2006, ApJL, 642, L81
Thomsen, M. 1985, Collisionless Shocks in the Heliosphere: Reviews of
  Current Research, Vol. 35, 253
Tsurutani, B. T., Ho, C. M., Arballo, J. K., Goldstein, B. E., & Balogh, A.
   1995, GeoRL, 22, 3397
Webb, G., Axford, W., & Terasawa, T. 1983, ApJ, 270, 537
Wei, W., Zhuang, B., Huang, J., et al. 2022, JGRA, 127, e2022JA030652
Woodham, L. D., Wicks, R. T., Verscharen, D., & Owen, C. J. 2018, ApJ,
Zank, G., Adhikari, L., Hunana, P., et al. 2017, ApJ, 835, 147
Zank, G., Li, G., Florinski, V., et al. 2004, JGRA, 109, A04107
Zank, G., Li, G., Florinski, V., et al. 2006, JGRA, 111, A06108
Zank, G., & Matthaeus, W. 1992, JGR, 97, 17189
Zank, G., Matthaeus, W., Bieber, J., & Moraal, H. 1998, JGRA, 103, 2085
Zank, G., Rice, W., & Wu, C. 2000, JGR, 105, 25079
Zank, G. I., Le Roux, J., Webb, G., Dosch, A., & Khabarova, O. 2014, ApJ,
Zank, G. P., & Matthaeus, W. 1993, PhFlA, 5, 257
Zhao, L., Li, G., Ebert, R., et al. 2016, JGRA, 121, 77
Zhao, L.-L., Adhikari, L., Zank, G., Hu, Q., & Feng, X. 2017, ApJ, 849, 88
Zhao, L.-L., Adhikari, L., Zank, G., Hu, Q., & Feng, X. 2018a, ApJ, 856, 94
Zhao, L.-L., Zank, G., Chen, Y., et al. 2019, ApJ, 872, 4
Zhao, L.-L., Zank, G., He, J., et al. 2021, A&A, 656, A3
Zhao, L.-L., Zank, G. P., Khabarova, O., et al. 2018b, ApJL, 864, L34
```